

On the fine structure of the quiet solar Ca II K atmosphere

A. Tritschler^{1,2,3}, W. Schmidt², H. Uitenbroek³, and S. Wedemeyer-Böhm²

¹ Big Bear Solar Observatory, New Jersey Institute of Technology, 40386 North Shore Lane, Big Bear City, CA-92314, USA
e-mail: ali@bbso.njit.edu, ali@kis.uni-freiburg.de, ali@nso.edu

² Kiepenheuer-Institut für Sonnenphysik, Schöneckstr. 6, 79104 Freiburg, Germany
e-mail: [wolfgang;wedemeyer]@kis.uni-freiburg.de

³ National Solar Observatory/Sacramento Peak*, PO Box 62, Sunspot, NM-88349, USA
e-mail: huitenbroek@nso.edu

Received 29 August 2005 / Accepted 23 October 2006

ABSTRACT

Aims. We investigate the morphological, dynamical, and evolutionary properties of the internetwork and network fine structure of the quiet sun at disk centre.

Methods. The analysis is based on a ~6 h time sequence of narrow-band filtergrams centred on the inner-wing Ca II K_{2v} reversal at 393.3 nm. To examine the temporal evolution of network and internetwork areas separately we employ a double-Gaussian decomposition of the mean intensity distribution. An autocorrelation analysis is performed to determine the respective characteristic time scales. In order to analyse statistical properties of the fine structure we apply image segmentation techniques.

Results. The results for the internetwork are related to predictions derived from numerical simulations of the quiet sun. The average evolutionary time scale of the internetwork in our observations is 52 s. Internetwork grains show a tendency to appear on a mesh-like pattern with a mean cell size of ~4–5 arcsec. Based on this size and the spatial organisation of the mesh we speculate that this pattern is related to the existence of photospheric downdrafts as predicted by convection simulations. The image segmentation shows that typical sizes of both network and internetwork grains are in the order of 1.6 arcsec.

Key words. Sun: chromosphere – Sun: oscillations

1. Introduction

The solar chromosphere is the highly structured and very dynamic atmospheric link between the photosphere and the thin transition layer to the hot corona. Understanding its physical structure is most likely to shed light on outer-atmosphere heating mechanisms and the acceleration and composition of the solar wind. Well known chromospheric diagnostics are the cores and inner wings of strong absorption lines like H α and Ca II H & K. Since the early work of Jensen & Orrall (1963), Orrall (1966), and Cram (1978) decades ago, the Ca II resonance lines have been extensively employed to explore chromospheric dynamics and chromospheric structure. For reviews and references therein we refer to Judge & Peter (1998) and Rutten (1999).

In low-spatial resolution filtergrams the internetwork regions appear rather homogeneous and dark, while the highly structured and inhomogeneous face of the chromosphere in the internetwork is only revealed in high-resolution filtergrams. Internetwork areas are intermittently filled with brightenings. These internetwork brightenings are most conspicuous in the emission feature in the blue wing of the Ca II K and H lines. Thus, they have been named Ca II K(H)_{2v} grains or simply *internetwork grains*. The investigation of the properties of these grains is a diagnostic tool to probe chromospheric conditions in internetwork regions. For a detailed description of the K_{2v} grain phenomenon we refer to Rutten & Uitenbroek (1991) and references therein.

Where does the intermittent chromospheric structure in space and time originate from? Observational evidence makes clear that the dynamic behaviour and radiative signature of the chromosphere is determined by its response to upward travelling waves (Wikstøl et al. 2000; Judge et al. 2001) excited by the effects of convection (Hoekzema & Rutten 1998; Skartlien et al. 2000; Hoekzema et al. 2002). While the waves propagate upwards they steepen into shocks and form high-frequency shock sequences pervading the internetwork regions. The formation of shocks is strongly supported by the numerical simulations of Carlsson & Stein (1992a,b, 1997). However, because of the one-dimensionality of these simulations, interference with slanted waves cannot be taken into account and shock trajectories are assumed to be radial. Recent three-dimensional radiative hydrodynamic simulations result in a dynamic and thermally bimodal structure of the non-magnetic chromospheric layers (Wedemeyer et al. 2004). The simulations show that upward travelling and interfering waves and shocks lead to the formation of a network of hot upwelling filaments and enclosed cool regions. The non-magnetic numerical modelling corroborates observational findings that the internetwork atmosphere and its behaviour are predominantly determined by the chromospheric response to acoustic oscillations.

Magnetic fields play a minor role in the internetwork grain generation (von Uexkuell & Kneer 1995; Remling et al. 1996; Hofmann et al. 1996; Steffens et al. 1996; Hoekzema & Rutten 1998; Lites et al. 1999; De Pontieu 2002; Hoekzema et al. 2002) and are only occasionally involved in form of the *flashers* (Brandt et al. 1992; Nindos & Zirin 1998; Krijger et al. 2001; de Wijn et al. 2005). However, magnetic fields appear to play

* Operated by the Association of Universities for Research in Astronomy, Inc. (AURA), for the National Science Foundation.

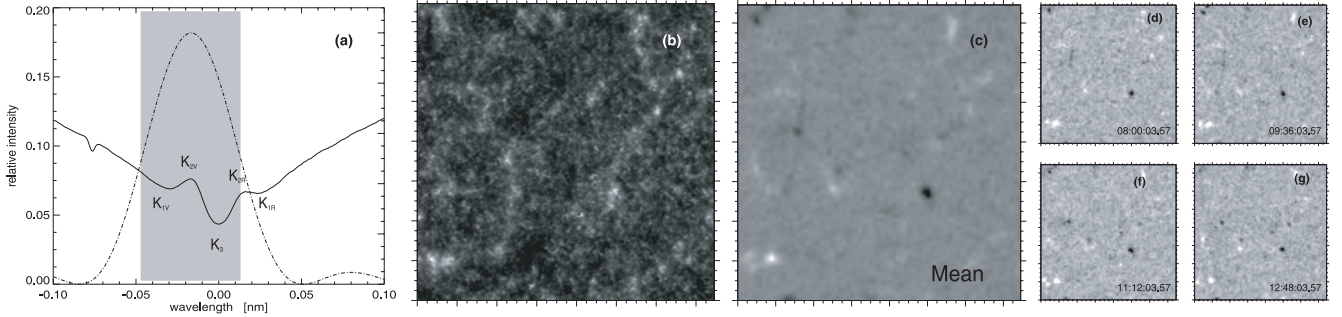


Fig. 1. **a)** Theoretical transmission curve of the Lyot filter (dot-dashed) and the mean spectrum of the Ca II K line taken from a photospheric spectral atlas (Neckel 1999). The shaded area indicates the 60 pm FWHM range. **b)** Best filtergram taken in the Ca II K line. One minor tick corresponds to 5 arcsec. The filtergram is displayed on a logarithmic scale. **c)–g)** Mean (large) and individual (small) magnetograms taken from MDI. One minor tick corresponds to 5 arcsec.

a major role in the higher atmosphere where plasma β (ratio of gas pressure over magnetic pressure) becomes small (McIntosh et al. 2001) and wave reflection and conversion between acoustic and magneto-acoustic modes takes place (Rosenthal et al. 2002; Bogdan et al. 2003).

In the present work we investigate the Ca II K chromosphere and its distinct fine structure based on an analysis of a long time sequence (~ 6 h) of narrow-band (60 pm FWHM) filtergrams featuring a spatial resolution of 0.7 arcsec. We concentrate on morphological, dynamical, and evolutionary differences between the network and the internetwork. We employ image segmentation techniques to establish statistics of properties like size and nearest-neighbour distance that can be used to validate current and future simulations.

The paper is organised as follows. The observations are introduced and the data reduction process is reviewed in Sects. 2 and 3, respectively. In Sect. 4 we go into image segmentation processing and describe the applied techniques (a) to distinguish on large-scales between the network and the internetwork, and (b) to identify and isolate small-scale chromospheric brightenings. In Sect. 5 the temporal evolution is studied as a result from a correlation analysis Sect. 6 is dedicated to a morphological analysis of chromospheric brightenings. The results of our investigation are concluded in Sect. 7.

2. Observations

The observations discussed here have been carried out at the Vacuum Tower Telescope of the Kiepenheuer-Institut at the Observatorio del Teide on Tenerife, May 7, 1999. A Halle Lyot filter was used to obtain narrow-band filtergrams in the Ca II K line at 393.3 nm. The width of the filter was set to 60 pm and the transmission band was centred ~ 0.017 nm away from line core on the K_{2v} emission reversal. A ~ 6 h sequence was recorded with a cadence of 6.04 s on a blue-sensitive 1024×1024 pixel CCD camera operated in a 512×512 summing mode. The resulting image scale on the detector was 0.35×0.35 arcsec²/pixel. The exposure time was 250 ms. For image stabilisation the VTT correlation tracker system was used (Schmidt & Kentischer 1995; Ballesteros et al. 1996). Figure 1a shows the atlas profile of the central part of the Ca II K line taken from Neckel (1999) and the theoretical transmission function of the Lyot filter. Figure 1b shows the best Ca II K filtergram of the observed quiet sun region. The observed intensities in the filtergram are dominated by the K_{2v} emission feature and contaminations from K_3 and K_{1v} are strongly suppressed due to the rather sharp decline of the transmission function. Even in case the K_{2v} reversal is absent,

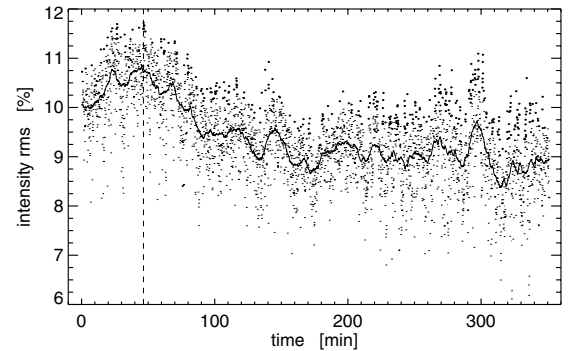


Fig. 2. Rms-intensity fluctuation as a function of time during the observation (small dots). Solid: smoothed version of the fluctuation used to determine all points that are $>7.5\%$ from the local average value (large dots). The vertical dashed line indicates the time where the best filtergram displayed in Fig. 1 was taken.

the main contribution to the integrated intensity comes from the range of heights that contribute to reversal features, although at a much reduced source function. The influence from red-shifted K_{1v} or blue-shifted K_3 is expected to be small within the 60 pm filter passband in our observations. To estimate the formation height range more quantitatively we performed a preliminary analysis employing response functions to examine the influence of temperature changes in the solar atmosphere on the filter integrated signal (see Fossum & Carlsson 2005). From the response functions computed through a hydrostatic model of the solar atmosphere we conclude that our filtergram observations basically reflect conditions prevailing in the height range 350–650 km. Experiments show that this height range is very similar in one-dimensional snapshots from simulations of chromospheric dynamics (e.g. Carlsson & Stein 1997). For a more thorough study of the influence of temperature changes in the solar atmosphere on the response of the filter integrated signal we refer to Uitenbroek (2006).

MDI on-board SoHO acquired magnetograms and continuum intensity data in the full-disk mode (2 arcsec spatial resolution) with a cadence of 96 min. These data were averaged in time, rescaled and co-aligned to the mean Ca II K filtergram averaged over the whole ~ 6 h observing period (Fig. 3, left). Figure 1c shows the resulting mean magnetogram and the four frames (d–g) taken during our observing period. The magnetograms show several magnetic elements up to the size of ~ 10 arcsec. These structures are persistent during the whole observation and coincide spatially with bright regions in Ca II K

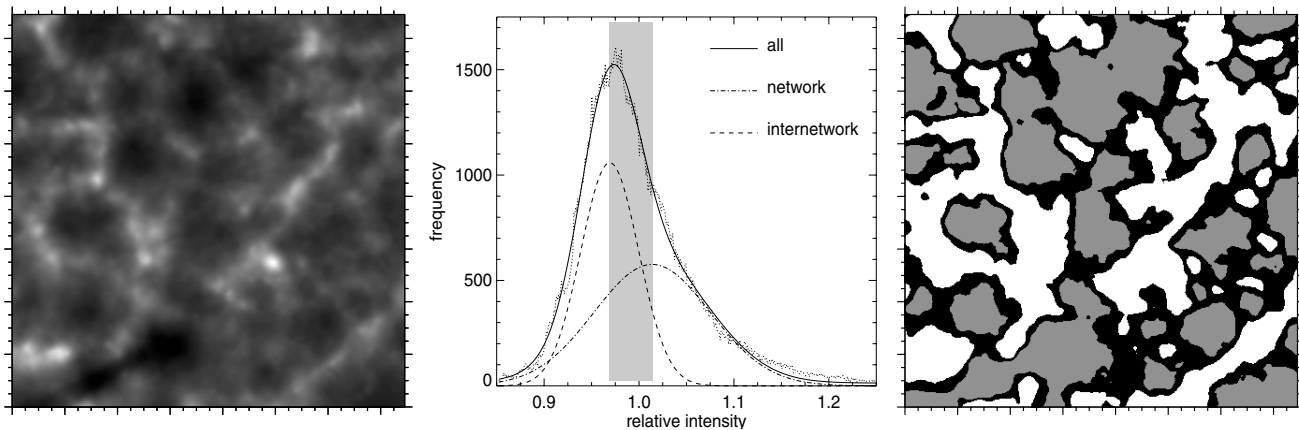


Fig. 3. *Left:* mean intensity map (averaged over the whole sequence). *Middle:* histogram of the mean intensity map (dotted), double-Gaussian fit to the data points (full) and single-Gaussian profiles (dashed, dashed-dotted). The shaded area indicates the range of relative intensities that is excluded from the statistical analysis. *Right:* masks used for the definition of the internetwork (grey) and the network (white). Black areas define regions which do neither belong to the network nor to the internetwork according to our definition.

outlining the chromospheric network (see Fig. 1b). The smallest structures visible in our data in the internetwork regions span 2–3 pixels corresponding to 0.7–1.0 arcsec. This puts an upper limit on the spatial resolution.

3. Data reduction

All data were corrected for dark current and offset and for intensity inhomogeneities caused by the CCD or any optical surface. The guiding was not perfect throughout the whole sequence; occasionally, the correlation tracker, working on normal granulation, lost its tracking position in moments of bad seeing. Therefore the images of the series were aligned by shifting and minimising the root-mean-square difference with a precision of about 0.2 pixel. To this end, every 100th image was selected as a reference image, and these images were aligned first. If the chosen reference image had poor contrast, we used a neighbouring, good-quality image instead. In a second step, the full sequence was then aligned with respect to the nearest reference image. The post-facto alignment procedure reduced the common field of view to about 150×150 arcsec². The remaining image displacements are below 1 pixel, and are mostly due to distortion within the field of view. They do not affect our data analysis.

To characterise the quality of our data set we computed the root-mean-square (rms) intensity contrast for each image, which is displayed in Fig. 2. The rms values fluctuate around a mean of $\sim 9\%$, with a maximum and minimum of almost 12% and 6%, reflecting the best and the worst moments, respectively.

4. Image segmentation

This section introduces the image segmentation methods we employ to determine statistical properties of internetwork and network fine structure (see Sect. 6). To distinguish between internetwork and network areas on large spatial scales we employ a threshold technique, and to identify and isolate individual bright structures on relatively small spatial scales, we apply morphological image processing techniques.

4.1. Definition of network and internetwork

We use the very different temporal behaviour of the network and the internetwork to distinguish between the two. After

normalising the intensities of each individual filtergram to the mean intensity of the image I_{mean} the mean intensity map (Fig. 3, left) was calculated by averaging over all 3483 single filtergrams. Motivated by the visual impression that the intensity map is dominated by two different populations of intensity we fitted the histogram (Fig. 3, middle) of the mean intensity map by a double-Gaussian function. The two maxima of the Gaussian components, located at 0.97 and 1.02, were used as intensity thresholds: pixels darker than <0.97 and brighter than >1.02 are considered as internetwork and network, respectively (see e.g. Kneer & von Uexkull 1993; Steffens et al. 1996; Krijger et al. 2001). The right panel of Fig. 3 shows the binary mask that results from thresholding the mean intensity map with the values provided by the double-Gaussian fit. White areas define network regions and grey areas define internetwork regions. Black areas are indefinite and are not included in the analysis described in Sects. 5 and 6. If not mentioned otherwise in the following all intensities are given in units of I_{mean} .

4.2. Morphological image processing

We pursue an image segmentation (or tessellation) approach to identify and isolate individual chromospheric brightenings in the network and the internetwork. We use an IDL implementation of the watershed transformation to segment each filtergram into watershed regions (cells) and their boundaries. As a result each individual cell harbours one maximum and thus isolates and defines a single structure. The transformation makes use of the morphological watershed operator labelling each watershed region with a unique index, and boundaries set to zero. For further details see Dougherty (1992). Prior to the image segmentation process an optimum filter is applied to each filtergram to suppress high-frequency noise and to avoid over-segmentation.

Figure 4 (left) visualises the tessellation for a sample filtergram. We estimated the background intensity of each identified structure inside the cell by averaging over the cell boundary contours. The number of cell pixels define the cell size and the average over these pixels defines the mean cell intensity. From the mean background intensity and the peak intensity we derive the full-width-half-maximum size (effective diameter) of the corresponding structure (see Tritschler & Schmidt 2002). Finally, each of the identified maxima are connected to its neighbouring maxima via a mathematical triangulation which returns an

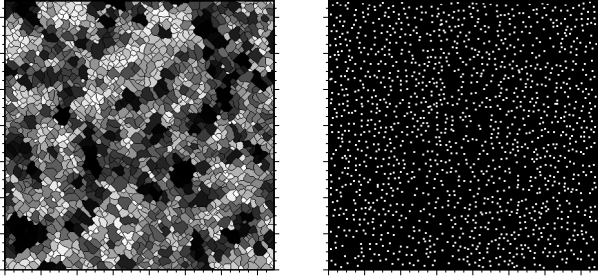


Fig. 4. *Left:* segmented image as a result from the watershed transformation. *Right:* binary mask indicating the intensity peak position of identified fine structure from the watershed transformation. For better visibility the positions are marked using more than one pixel.

adjacency list from which nearest-neighbour distances can be computed directly.

In addition we determine all local maxima along each intensity row and column via numerical differentiation. Local maxima in the image are then found by identifying all the pixels where local maxima in row and column coincide. A comparison shows that these local maxima match very well with those found using the watershed transformation. Although the peak intensity is determined by the image segmentation process we do not evaluate on the statistics of those but use it only for thresholding purposes.

5. Temporal evolution of the chromosphere

In the following, we analyse the temporal evolution of the chromospheric network and internetwork regions. First, we deduce characteristic time scales for the network and internetwork, separately. Second, the results from the segmentation processing are used to visualise and study the appearance of the fine structure. Third, we examine the temporal and spatial frequency behaviour using the $k - \nu$ -diagram as well as power maps as a diagnostic tool.

5.1. Autocorrelation analysis

In order to specify the temporal evolution in more detail characteristic time scales are derived from an autocorrelation analysis. To compare with the numerical results of Wedemeyer et al. (2004) the whole field-of-view is divided into 22×22 pixel subfields with 50% overlap so that the subfield size corresponds to the simulation size which covers a $\sim 5.6 \times 5.6 \text{ Mm}^2$ region of the quiet Sun horizontally. Each individual subfield is allocated to the network or to the internetwork if 100% of the pixels coincide with network or internetwork pixels as defined by a mask similar to the one described in Sect. 4.1 but using an intensity map averaged over ~ 75 min (instead of the full ~ 350 min). For computational reasons we performed the autocorrelation analysis for all subfields on the first 750 images (~ 75 min) only, which provides a statistical relevance of the autocorrelation function up to 25 min.

In Fig. 5 each single autocorrelation function is plotted as a function of time for all internetwork (upper panel) and network (lower panel) subfields, revealing a diversity in amplitude and phase. We highlight the autocorrelation of two individual subfields in the internetwork and network (dash-dotted) to demonstrate that their behaviour stays quasi-periodic for a time lag of at least 25 min. For both the network and the internetwork, the first cycle in the individual and the average autocorrelation peaks

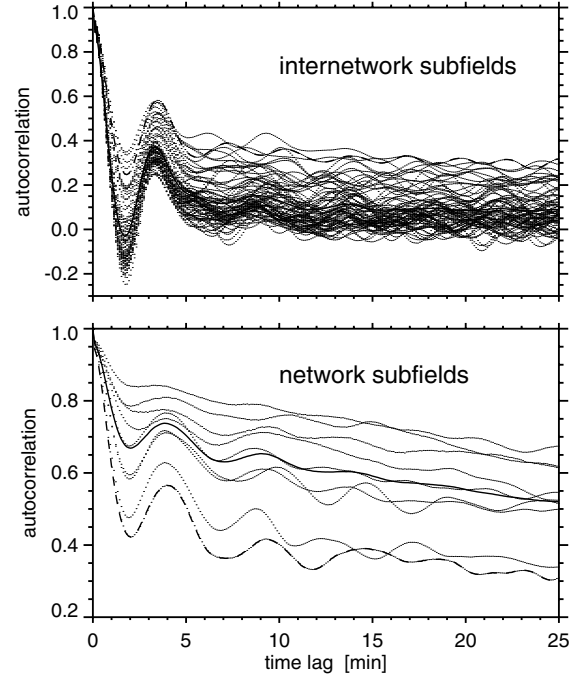


Fig. 5. Autocorrelation versus time. Dots: individual autocorrelation functions for all subfields that belong either to the internetwork (*upper panel*, 73 subfields corresponding to the filled circles in Fig. 6, right) or to the network (*lower panel*, 10 subfields corresponding to the open circles in Fig. 6, right). Thick solid: average over all network/internetwork subfields. Thick dash-dotted: individual autocorrelation functions.

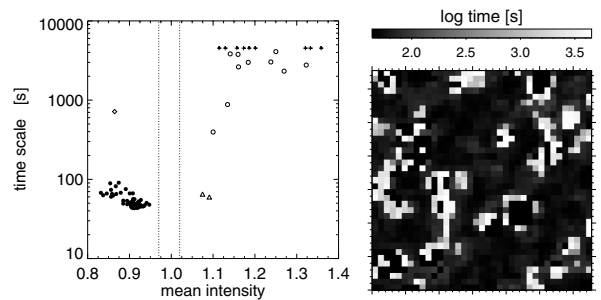


Fig. 6. *Left:* evolutionary time scale versus mean intensity. Vertical dotted lines indicate the intensity threshold chosen to differ between internetwork (filled circles) and network (open circles) subfields. Diamond: internetwork subfield with comparably long time scale. Triangles: network subfields with comparably short time scales. Crosses: network subfields with time scales longer than the duration of the used data set (see text). *Right:* evolutionary time scale per subfield.

at ~ 3 min. The following cycles tend to appear with a 3–4 min period for internetwork subfields and with a ~ 5 min period for network subfields.

As an evolutionary time scale we take the time after which the autocorrelation decreased to a value of $1/e$. For those subfields where the autocorrelation function does not fall below a value of $1/e$, the time scale is set to the duration of the chosen data set of 4530 s. Figure 6 shows the derived time scale versus the mean intensity per subfield (left), and a spatial map of all deduced time scales (right). The time scales show a clear dichotomy between network and internetwork subfields. The internetwork time scales group together in the range 43–91 s with a mean of 52 s. In taking this mean we neglect one out of the 74 internetwork subfields that shows a much larger time scale of

716 s, most likely due to contributions of unresolved magnetic elements. We cannot evaluate the proper mean time scales for the network subfields because of the time constraint of ~ 75 min (see above). However, network time scales are well known to vary substantially in the range from min to many hours (e.g. Liu et al. 1994; Muller 1994; Berger & Title 1996; Berger et al. 1998; Nisenson et al. 2003).

Comparison with simulations. Evolutionary time scales based on horizontal cross-sections of gas temperature at fixed geometrical heights in the 3D hydrodynamical simulations of Wedemeyer et al. (2004) of the quiet sun are height dependent with values in the range 20–25 s at chromospheric heights (~ 1000 km) and about 70 s in the middle photosphere (Wedemeyer 2003). The temperature amplitudes of the model chromosphere might be somewhat uncertain due to the simplified treatment (grey, LTE), whereas the dynamics and the related timescales are connected to already realistically modelled lower layers. An indirect qualitative comparison can be done if one considers the following effects: (a) the observed intensity originates from an extended formation height range instead of a fixed geometrical height, (b) intensities refer to corrugated surfaces of optical depth instead of plane horizontal cuts like used for the model, (c) observations are subject to seeing (spatial smearing) and instrumental effects, in particular spatial resolution, (d) the simulations cover horizontally a limited range of ~ 6 Mm only and do not account for dynamic phenomena larger than these scales, (e) the simulations are purely hydrodynamic. The mean value of 52 s derived from our observations is too short for being due to reversed granulation in the middle photosphere (70 s in the model) but, considering the mentioned effects, is actually in a plausible range expected for (low) chromospheric layers.

5.2. Image segmentation analysis

We turn now to the question whether the internetwork brightenings occur at preferred locations. We use the image segmentation processing that provides a list of positions of all identified brightenings, and compute the cumulative bright point number in dependence of integration time. Figure 7 (upper panels) shows the result for an integration time of 350 min. We display two maps: if all the brightenings are taken into account (left) and only those that have intensities $> 1.2 I_{\text{mean}}$ (right). For better visibility of the internetwork regions the cumulative maps are displayed on a logarithmic scale. The top left panel of Fig. 7 shows locations that are void of brightenings during the whole observing time. These are locations close-by the network and around strong magnetic elements where almost no brightenings appear nor move to. The map with an intensity threshold value of $1.2 I_{\text{mean}}$ (Fig. 7, upper panel, right), shows that there are also internetwork regions with a deficit in the occurrence of brightenings like the one in the lower left part of our FOV (extending 70 arcsec in x -direction and 40 arcsec in y -direction). We cannot exclude completely that these internetwork regions directly surrounding the network are a byproduct of the image segmentation process. Network bright points appear to be diffuse in intensity because of scattering effects in the solar atmosphere. As a consequence localised peaks produced by internetwork grains moving towards or emerging close by the network are harder to detect against the diffuse halo around the network bright points which results in a deficit of detected brightenings. The lower panel of Fig. 7 shows a zoom-in into the cumulative maps for integration times of 3 min (left) and 10 min (right). We recognise a regular

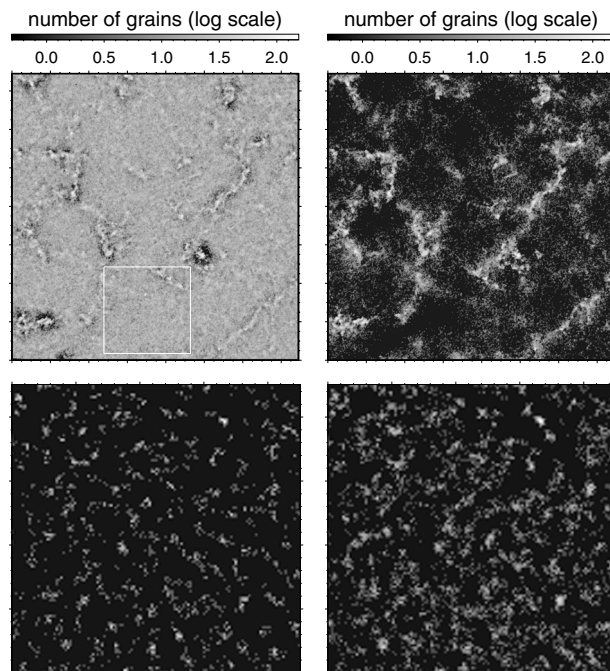


Fig. 7. Upper panels: cumulative number of bright points after an integration time of 350 min (left) and with a threshold intensity of $> 1.2 I_{\text{mean}}$ (right). One minor tick corresponds to 5 arcsec. Lower panels: zoom-in (by a factor of two) into the cumulative number of bright points (at coordinates $X = 48\text{--}93$ arcsec and $Y = 4\text{--}49$ arcsec as indicated by the white square in the upper panel, left) after 3 min (left) and 10 min (right) of integration. One minor tick corresponds to 2 arcsec.

mesh-like pattern in the internetwork which is still clearly visible after an integration time of up to ~ 10 min (a typical granular life time). The brightenings though appear to be mostly clustered on the nodes of this mesh. Even after an integration time of 60 min (not shown) the mesh is still distinctive. On average, the cell size of the mesh is $\sim 4\text{--}5$ arcsec. Since we mark the position of each brightening detected in every successive filtergram, the cumulative maps do reflect not only the appearance of a new internetwork grain but also the movement of those grains (due to seeing and proper motion) that have been detected before. A movie made of 3 min cumulative maps, shows evidence that the mesh pattern itself develops and migrates.

What is the physical mechanism that causes the bright grains to appear on an organised mesh? Simulations of solar convection show the organisation of strong downdraft fingers on a similar spatial scale (Stein & Nordlund 1989). Strong turbulence is associated with these downdrafts. According to Rimmele et al. (1995) this turbulence gives rise to acoustic noise, which is a potential source for the Ca II K_{2v} excitation. This would explain that the grains appear preferentially on a meso scale dictated by the downdraft fingers. The locations with a high number of accumulated bright points (brightest areas in Fig. 7, lower left panel) may well correspond to locations of such strong downdrafts. The bright points that appear in other locations may be generated by weaker turbulence in the more pronounced intergranular lanes that outline the meso-scale downflow pattern. The latter could explain the slow migration of the pattern on time scales corresponding to granular evolution while the changes in the location of the more persistent bright points corresponds to the times over which the meso-scale downflows evolve. Note, however, that there is not necessarily a one-to-one correspondence between

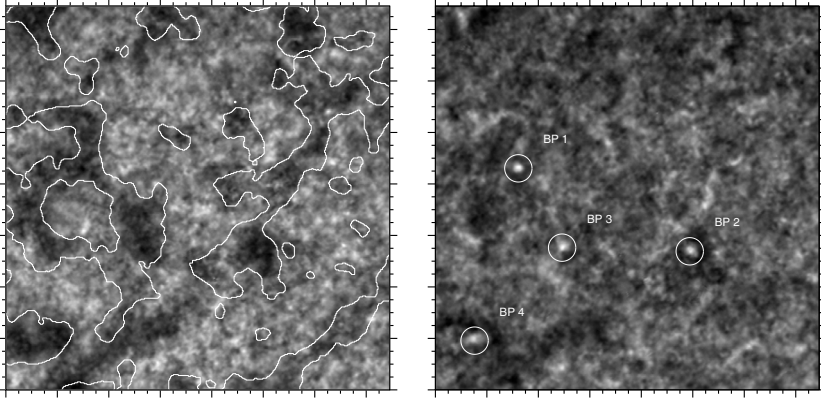


Fig. 8. Power maps with 3 min (*left*) and 5 min (*right*) periodicity computed over the full 6 hours. The contour lines in the 3 min power map outline the network as determined from the intensity map averaged over the whole time sequence. The images are scaled independently. One minor tick mark corresponds to 5 arcsec. Circles indicate locations with increased signal in the 5 min band that are co-located with enhanced magnetic signal in the average MDI magnetogram (see Fig. 1, c).

the location of the photospheric excitation and the resulting occurrence of a bright point (Hoekzema et al. 1998; Hoekzema & Rutten 1998; Leenaarts & Wedemeyer-Böhm 2005) because the waves may not propagate vertically.

5.3. Power maps

We compute the power over the ~ 6 hours at each pixel and apply a bandpass filter to extract the contributions from signal with a 3 min and 5 min periodicity. The bandpass filters are centred at 5.5 mHz and 3.33 mHz, with a FWHM of 0.4 mHz each. Large-scale intensity variations in time are eliminated by a linear fit to the data points. To apodise we apply a one-dimensional Hanning window function that covers 8% of the data vector length and tapers the edges to zero.

Figure 8 shows the resulting power maps thus visualising the well-established effect that internetwork and network respond in a different way to wave motions most likely excited in the photosphere (Liu & Sheeley 1971; Cram & Dame 1983; Dame et al. 1984; Lites et al. 1993, 1994; Judge et al. 2001). The network participates predominantly in long-period oscillations (>5 min) while in the internetwork short-period oscillations (~ 3 min, and shorter) dominate the picture.

From the 3 min map we recover that there are regions that according to our definition clearly belong to the internetwork, but show a significant suppression of 3 min power. The most conspicuous area is the slanted one between $X = 20\text{--}70$ arcsec and $Y = 0\text{--}35$ arcsec (also apparent in Figs. 3, left, and 7, upper panel, left). These voids have been observed before (e.g. Judge et al. 2001; Krijger et al. 2001) and named *magnetic shadows* by Judge et al. (2001). The phenomenon is ascribed to the spreading of the magnetic field with height and forming the canopy, shadowing its immediate surroundings and thus hampering (or modifying) upward propagating waves (see also Rosenthal et al. 2002; Bogdan et al. 2003). The shadows also appear around strong network bright points with a persistent magnetic signal as can be seen in the right panel of Fig. 8 and in addition as narrow lanes along the network as indicated by the map of the cumulative number of bright points (see Fig. 7, upper panel, left). Inspecting the radial behaviour of azimuthally averaged power spectra from the centre of the indicated network bright points (BP1-BP4 in Fig. 8, right) outwards we find the tendency that the integrated power is sharply decreasing with distance giving rise to the shadows around the bright points. Power increases again to average levels in the internetwork beyond the indicated circles.

6. Morphology

The results of image segmentation are visualised in terms of occurrence distributions separately for the internetwork and the network. Our network and internetwork masks (Sect. 4.1) avoid regions that show mean intensities between $0.97 < I_{\text{mean}} < 1.02$ by definition. For comparison, we also show the occurrence distribution representative for all identified brightenings inside the FOV. Note that these occurrence distributions include brightenings with $0.97 < I_{\text{mean}} < 1.02$. Each occurrence distribution is normalised to the total number of identified brightenings.

Since we do not track each individual identified brightening in time, our sample of brightenings is not statistically independent. Therefore, and to be more independent from seeing conditions, only those filtergrams contribute to the distributions, that show a rms-contrast of 7.5% higher than the value of a smoothed version of the contrast variation at the same time step (see Fig. 2). This leads to a selection of 360 filtergrams with a mean cadence of 57 s (not equidistant). We count only those structures that span more than two pixels in both cell size and effective diameter, and that have nearest-neighbour distances larger than 3 pixels. This leaves us with a sample of 206056 identified structures.

6.1. Size distributions

The image segmentation techniques (see Sect. 4) are used to derive three different size measures: effective diameters, cell sizes, and mean distances to next neighbour elements. Figure 9 displays the resulting occurrence distributions. They are single-peaked and asymmetric with a steep rise to the peak, followed by a gradual fall-off with size. All size measures peak almost at equal values for the network and the internetwork: we find typical effective diameters of 1.6 arcsec for both internetwork and network structures. We partly ascribe this to the limitations of the image segmentation process. Characteristic cell sizes are almost twice as large as effective diameters and peak around 2.8 arcsec and 3.0 arcsec while nearest-neighbour distances are typically 4.0 arcsec and 4.2 arcsec for the internetwork and network, respectively. Arithmetic mean values are larger than the characteristic values since they reflect the asymmetry of the corresponding distribution function. The mean value for the nearest-neighbour distance in the internetwork amounts to 5 arcsec quantifying and confirming the impression we got from the cumulative bright point number maps (see Fig. 7) that reveal the existence of a $\sim 4\text{--}5$ arcsec (judged by eye) mesh-like pattern in the internetwork.

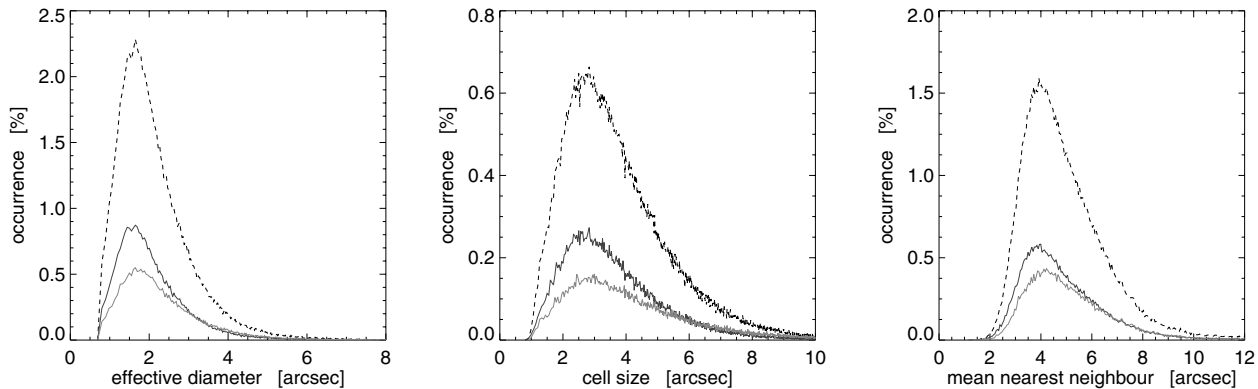


Fig. 9. Occurrence distributions of the effective diameter (*left*), the cell size (*middle*), and the nearest neighbour distance (*right*). The distributions are normalised with respect to the corresponding number of identified brightenings. For each quantity the distributions for the network (grey), the internetwork (black), and all identified structures (dashed) are displayed.

6.2. Discussion

The simulations of Carlsson & Stein (1997) do reproduce the spectral and temporal behaviour of the Ca II H line profile quite well but are one-dimensional and thus cannot predict morphological properties. On the other hand, current three-dimensional radiative hydrodynamic simulations (Wedemeyer et al. 2004) have to neglect time-dependent Hydrogen ionisation and non-grey NLTE radiative transfer, so that no realistic Ca II K line profiles can be synthesised.

Seeing conditions, differential image motion, and instrumental effects influence the spatial resolution and thus affect the image segmentation algorithm. We resolve structures that are larger than 0.7 arcsec. Spatially unresolved conglomerates of small structures are interpreted as a large single structure, which leads to an underestimation of the frequency of small-scale brightenings. We argue that this is predominantly the case for the internetwork. It is most likely that we predominantly detect the brightest structures and are unable to resolve their substructure. Underestimation of the occurrence of faint structures on the one side and not resolving the substructure of the rare brightest structures shifts e.g. the peak of the size distributions to larger scales. This might explain the similarities found in the size distribution functions of the network and the internetwork. To clarify this data sets with better spatial resolution are needed.

What is the physical mechanism that causes the bright grains to appear on an organised mesh (see Sect. 5.2)? Simulations of solar convection show the organisation of strong downdraft fingers on a similar spatial scale (Stein & Nordlund 1989). Strong turbulence is associated with these downdrafts. According to Rimmele et al. (1995) this turbulence gives rise to acoustic noise, which is a potential source for the Ca II K_{2v} excitation. This would explain that the grains may appear preferentially on a meso scale dictated by the downdraft fingers. The locations with a high number of accumulated bright points (brightest areas in Fig. 7, lower left panel) may well correspond to locations of such strong downdrafts. The bright points that appear in other locations may be generated by weaker turbulence in the more pronounced intergranular lanes that outline the meso-scale downflow pattern. The latter could explain the slow migration of the pattern on time scales corresponding to granular evolution while the changes in the location of the more persistent bright points corresponds to the times over which the meso-scale downflows evolve. Note, however, that there is not necessarily a one-to-one correspondence between the location of the photospheric

excitation and the resulting occurrence of a bright point (Hoekzema et al. 1998; Hoekzema & Rutten 1998; Leenaarts & Wedemeyer-Böhm 2005) because the waves may not propagate vertically.

7. Conclusions

We analysed a long time sequence of narrowband Ca II K filtergrams to investigate the morphological, dynamical, and evolutionary properties of the solar chromosphere separately for the internetwork and the network. Quantifying these properties is important for comparison with current and future numerical simulations.

From an autocorrelation analysis on small subfields we find average evolutionary time scales of 52 s in the internetwork. Individual values can be found in the range 40–90 s. The predicted time scales of temperature variations in the numerical simulations compare favourably with the observed time scales of intensity variations in the internetwork notwithstanding the severe simplifications in the simulations. Differences between the two time scales may occur because of intensity variations are the result of variations of temperatures over a range of optical depths and these vary with height themselves. In addition, seeing and instrumentation affect the spatial resolution leading to longer time scales.

To identify and isolate small-scale features we apply image segmentation techniques and find evidence for internetwork grain patterning on spatial scales of ~ 4 –5 arcsec (see Sect. 5.2, Fig. 7). We argue that this pattern is related to photospheric downdrafts, which occur on similar spatial scales, through the enhanced excitation of acoustic waves that these downdrafts provide.

We separated network from the internetwork by a double-Gaussian decomposition of the intensity distribution averaged over the full duration of the observation. The validity of this decomposition is confirmed by the 3 min power map (Fig. 8, left) in which the power deficit on the network coincides almost perfectly with the network mask. There is, however, one region (lower left) that appears dark in both the mean intensity map (Fig. 1, left) and the 3 min power map. We speculate that this region contains magnetic field that has not penetrated yet into the chromosphere. Either the magnetic field hinders the propagation of acoustic waves or these waves suffer mode conversion at low altitude before giving rise to Ca II K emission. The latter

is also the mechanism proposed for the small-scale shadows we see around strong network bright points (Fig. 8, right).

From a statistical analysis based on results from image segmentation we find that internetwork grains and network bright points appear to have very similar typical sizes (~ 1.6 arcsec). This is somewhat surprising because of their different physical nature as is evident from differences in the power spectra and the disparity in their temporal behaviour. We surmise that this has to be attributed in part to insufficient spatial resolution.

For better understanding of the statistical properties in the Ca II K filtergrams and how they are related to physical properties in the solar atmosphere both simulations that allow realistic modelling the formation of Ca II K, and observations with higher spatial and spectral resolution are required, preferably in the form of two-dimensional spectroscopy.

Acknowledgements. The VTT is operated by the Kiepenheuer-Institut für Sonnenphysik, Freiburg, Germany. Part of this work (A.T.) was supported by the DFG under grant, by NSF under grants ATM 00-86999 and AST MRI 00-79482, and by NASA under grant NAG 5-12782. We thank the referee Rob Rutten for extensive comments.

References

- Ballesteros, E., Collados, M., Bonet, J. A., et al. 1996, *A&ASS*, 115, 353
 Berger, T. E., & Title, A. M. 1996, *ApJ*, 463, 365
 Berger, T. E., Loefeldahl, M. G., Shine, R. S., & Title, A. M. 1998, *ApJ*, 495, 973
 Bogdan, T. J., Hansteen, M. C. V., McMurry, A., et al. 2003, *ApJ*, 599, 626
 Brandt, P. N., Rutten, R. J., Shine, R. A., & Trujillobueno, J. 1992, in *Cool Stars, Stellar Systems, and the Sun*, ASP Conf. Ser., 26, 161
 Carlsson, M., & Stein, R. 1992a, in *Cool Stars, Stellar Systems, and the Sun*, ASP Conf. Ser., 26, 515
 Carlsson, M., & Stein, R. F. 1992b, *ApJ*, 397, L59
 Carlsson, M., & Stein, R. F. 1997, *ApJ*, 481, 500
 Cram, L. E. 1978, *A&A*, 70, 345
 Cram, L. E., & Dame, L. 1983, *ApJ*, 272, 355
 Dame, L., Gouttebroze, P., & Malherbe, J.-M. 1984, *A&A*, 130, 331
 De Pontieu, B. 2002, *ApJ*, 569, 474
 de Wijn, A. G., Rutten, R. J., Haverkamp, E. M. W. P., & Sütterlin, P. 2005, *A&A*, 441, 1183
 Dougherty, E. R. 1992, in *An Introduction to Morphological Image Processing*, ed. E. R. Dougherty, SPIE-International Society for Optical Engineering
 Fossum, A., & Carlsson, M. 2005, *ApJ*, 625, 556
 Hoekzema, N. M., & Rutten, R. J. 1998, *A&A*, 329, 725
 Hoekzema, N. M., Rutten, R. J., Brandt, P. N., & Shine, R. A. 1998, *A&A*, 329, 276
 Hoekzema, N. M., Rimmele, T. R., & Rutten, R. J. 2002, *A&A*, 390, 681
 Hofmann, J., Steffens, S., & Deubner, F.-L. 1996, *A&A*, 308, 192
 Jensen, E., & Orrall, F. Q. 1963, *ApJ*, 138, 252
 Judge, P. G., & Peter, H. 1998, *Space Sci. Rev.*, 85, 187
 Judge, P. G., Tarbell, T. D., & Wilhelm, K. 2001, *ApJ*, 554, 424
 Kneer, F., & von Uexkull, M. 1993, *A&A*, 274, 584
 Krijger, J. M., Rutten, R. J., Lites, B. W., et al. 2001, *A&A*, 379, 1052
 Leenaarts, J., & Wedemeyer-Böhm, S. 2005, *A&A*, 431, 687
 Lites, B. W., Rutten, R. J., & Kalkofen, W. 1993, *ApJ*, 414, 345
 Lites, B. W., Rutten, R. J., & Thomas, J. H. 1994, in *Solar Surface Magnetism*, 159
 Lites, B. W., Rutten, R. J., & Berger, T. E. 1999, *ApJ*, 517, 1013
 Liu, S. Y., & Sheeley, N. R. 1971, *Sol. Phys.*, 20, 282
 Liu, Y., Zhang, H., Ai, G., Wang, H., & Zirin, H. 1994, *A&A*, 283, 215
 McIntosh, S. W., Bogdan, T. J., Cally, P. S., et al. 2001, *ApJ*, 548, L237
 Muller, R. 1994, in *Solar Surface Magnetism*, 55
 Neckel, H. 1999, *Sol. Phys.*, 90, 421
 Nindos, A., & Zirin, H. 1998, *Sol. Phys.*, 179, 253
 Nisenson, P., van Ballegoijen, A. A., de Wijn, A. G., & Sütterlin, P. 2003, *ApJ*, 587, 458
 Orrall, F. Q. 1966, *ApJ*, 143, 917
 Remling, B., Deubner, F.-L., & Steffens, S. 1996, *A&A*, 316, 196
 Rimmele, T. R., Goode, P. R., Harold, E., & Stebbins, R. T. 1995, *ApJ*, 444, L119
 Rosenthal, C. S., Bogdan, T. J., Carlsson, M., et al. 2002, *ApJ*, 564, 508
 Rutten, R. J. 1999, in *Third Advances in Solar Physics Euroconference: Magnetic Fields and Oscillations*, ASP Conf. Ser., 184, 181
 Rutten, R. J., & Uitenbroek, H. 1991, *Sol. Phys.*, 134, 15
 Schmidt, W., & Kentischer, T. 1995, *A&AS*, 113, 363
 Skartlien, R., Stein, R. F., & Nordlund, Å. 2000, *ApJ*, 541, 468
 Steffens, S., Hofmann, J., & Deubner, F. L. 1996, *A&A*, 307, 288
 Stein, R. F., & Nordlund, A. 1989, *ApJ*, 342, L95
 Tritschler, A., & Schmidt, W. 2002, *A&A*, 388, 1048
 Uitenbroek, H. 2006, in *Solar MHD: Theory and Observations - a High Spatial Resolution Perspective*, ed. H. Uitenbroek, J. Leibacher, & R. Stein, ASP Conf. Ser., 354
 von Uexkuell, M., & Kneer, F. 1995, *A&A*, 294, 252
 Wedemeyer, S. 2003, in *Ph.D. Thesis, University of Kiel*, ed. http://e-diss.uni-kiel.de/diss_764/
 Wedemeyer, S., Freytag, B., Steffen, M., Ludwig, H.-G., & Holweger, H. 2004, *A&A*, 414, 1121
 Wikstøl, Ø., Hansteen, V. H., Carlsson, M., & Judge, P. G. 2000, *ApJ*, 531, 1150